Air- and water-resistant noble metal coated ferromagnetic cobalt nanorods

Sergio Lentijo, Reasmey Phary Tan, Cécile Marcelot, Thomas Altantzis, Pier-Francesco Fazzini, Teresa Hungría, Benoit Cormary, James R. Gallagher, Jeffrey T Miller, Hervé Martinez, et al.

▶ **To cite this version:**

Sergio Lentijo, Reasmey Phary Tan, Cécile Marcelot, Thomas Altantzis, Pier-Francesco Fazzini, et al.. Air- and water-resistant noble metal coated ferromagnetic cobalt nanorods. ACS Nano, 2015, 9 (3), pp.2792–2804. 10.1021/nn506709k . hal-01503972

HAL Id: hal-01503972
https://hal.science/hal-01503972

Submitted on 5 Mar 2018

HAL is a multi-disciplinary open access archive for the deposit and dissemination of scientific research documents, whether they are published or not. The documents may come from teaching and research institutions in France or abroad, or from public or private research centers.

L'archive ouverte pluridisciplinaire **HAL**, est destinée au dépôt et à la diffusion de documents scientifiques de niveau recherche, publiés ou non, émanant des établissements d'enseignement et de recherche français ou étrangers, des laboratoires publics ou privés.

Air- and water-resistant ferromagnetic cobalt nanorods

Sergio Lentijo-Mozo[1], Reasmey P. Tan[1], Cécile Garcia-Marcelot[1,2], Thomas Altantzis[3], Pier-Francesco Fazzini[1], Teresa Hungria[1], Benoit Cormary[1], James R. Gallagher[4], Jeffrey T. Miller[4], Hervé Martinez[5], Marc Respaud[1], Sara Bals[3], Gustaaf Van Tendeloo[3], Christophe Gatel[2], and Katerina Soulantica[1*]

[1] Laboratoire de Physique et Chimie des Nano-objets (LPCNO), Université de Toulouse; INSA, UPS, CNRS, 135 avenue de Rangueil, 31077 Toulouse (France)

[2] Centre d'Elaboration de Matériaux et d'Etudes Structurales (CEMES-CNRS), 29 rue Jeanne Marvig, B.P. 94347, 31055 Toulouse (France)

[3] Electron Microscopy for Materials Research (EMAT), University of Antwerp, Groenenborgerlaan 171, 2020 Antwerp, (Belgium)

[4] Chemical Science and Engineering Division, Argonne National Laboratory, 9700 S Cass Ave., Argonne, IL, 60439 (USA)

[5] IPREM-ECP CNRS UMR 5254, Université de Pau, Hélioparc Pau Pyrénées, 2 av. Pierre Angot, 64053 Pau Cedex 9, France

Cobalt nanorods possess ideal magnetic properties for applications requiring hard magnetic nanoparticles. However, their exploitation is undermined by their sensitivity towards oxygen and water, which deteriorates their magnetic properties. The development of a continuous metal shell inert to oxidation could render them stable, opening new perspectives not only for already identified applications but also for new uses. However, the direct growth of a conformal noble metal shell on magnetic metals is a challenge. Here, we show that prior treatment of Co nanorods with a tin coordination compound enables the growth of a continuous noble metal shell, rendering them air and water-resistant. The as-synthesized core-shell nanoparticles are the first, ferromagnetic nanorods that combine high magnetization and strong uniaxial magnetic anisotropy, even after exposure to air and water, and hold promise for successful implementation in new domains such as *in vitro* bio-diagnostics requiring probes of high magnetization and an anisotropic shape.

An important research activity in nanoscience concerns the development of magnetic nano-objects, prepared by solution chemical analysis[1-4]. Among them, metallic Co single-crystalline nanorods (Co-NRs) of hexagonal close packed structure[5], exhibit particularly attractive magnetic properties[6] for implementation in domains requiring materials with both high magnetization and high coercivity[7,8]. However, the practical use of metallic magnetic nano-objects in general, is undermined by their reactivity towards oxygen and water, which transforms them into the corresponding oxides and/or hydroxides deteriorating their magnetic properties. Protection of air-sensitive metallic magnetic nanoparticles against oxidation can be achieved through an efficient coating by an adequate layer[3,9-11]. However, air- and water-resistant ferromagnetic nanorods of a high magnetic moment have never been reported up to now. A noble metal shell may not only act as an efficient barrier to oxidation, but also add its specific properties to those of the core, or become a platform for further surface

functionalization[3,12-14]. Gold is an ideal shell material because it is chemically stable, optically active and can be easily bio-functionalized. Pt is also chemically inert and despite the fact that its optical properties are less interesting compared to those of Au, it is a highly active metal in catalysis[15-17]. The development of a conformal shell of a material on a seed nanocrystal depends on many parameters which affect the interplay between surface and interface energies, and therefore the final result[18-21]. For colloidal nanocrystals, the presence of ligands, necessary to ensure a good dispersion and therefore a homogeneous reaction with the shell precursor, may substantially alter surface and interfacial energies, but may also hamper seed-surface accessibility, preventing a homogeneous shell formation[21,22]. It is furthermore important to stress that when noble metal ions come into contact with nanocrystals of a less noble metal, galvanic displacement may occur, partially dissolving the seed and reducing its dimensions[18]. Some reports in the literature describe Co@Au and Co@Pt core@shell superparamagnetic spherical nanoparticles[23-25]. To the best of our knowledge, Co@M nanorods (M = noble metal) have not been reported so far. The growth of a conformal shell on nanorods is more complicated in comparison to isotropic nanocrystals, since it requires a homogeneous "wetting" of the various crystal facets despite their different reactivity[18,21]. Cobalt is not a target metal for *in vivo* biomedical applications due to its toxicity. However, the field of *in vitro* bio-diagnostics does not suffer from this inconvenience and cobalt could respond to the specific needs of targeted biomedical applications, such as the magneto-optical *in vitro* detection of important biomarkers in physiological liquid samples[26]. Therefore, the growth of a protective shell opens the way to a successful implementation of highly performant, albeit up to now inexploitable in biomedical diagnosis, magnetic metallic nanoparticles. Apart from this specific application, protection of the Co core will also facilitate the implementation of the core-shell nanorods in magnetic recording[27], magnetically actuated liquid crystals[28], or ferrofluids[29].

Here we show that while direct noble metal deposition on Co-NRs fails to form a continuous shell, a simple treatment of the Co-NRs with a Sn(II) coordination compound enables the subsequent development of a continuous noble metal shell of Au and Pt on Co-NRs[30], rendering them air- and water-resistant. The present method should be generally applicable to metallic magnetic nanoparticles of various shapes, not only for protection purposes but also for obtaining performant and cost-efficient core-shell catalysts[31,32].

Gold-tipped as well as gold decorated Co-NRs have already been synthesized by using bare Co-NRs as seeds[33]. In both cases Au is epitaxially grown on the Co-NRs. Based on these results, we tried to develop a gold shell surrounding preformed Co-NRs, prepared by slight modifications of an already published method[5] (see details in Supplementary Information). However, all attempts have failed to cover the Co surface (Supplementary Fig. S1). In the best cases where Au growth was not limited to the tip area, a growth mode analogous to a Volmer-Weber (VW) epitaxial growth mode takes place[34,35], favoring small Co-Au interfaces instead of extended interfaces required for the formation of a complete shell.

Platinum is also resistant towards oxidation and has the advantage of being miscible with Co. Thus, provided that mild temperatures are employed during Pt overgrowth in order to avoid alloy formation, the growth of a continuous Pt shell around Co should be more favorable than in the case of Au. We attempted to grow Pt directly on Co-NRs by reducing the organometallic precursor [$PtMe_2COD$] (Me = methyl; COD= cyclooctadiene) in the presence of hexadecylamine (HDA) as a nanorod dispersant. Under all reaction conditions employed, a continuous Pt layer was not achieved. Independent Pt nucleation in solution was dominant, and in some cases we detected Pt “patches” on Co (Supplementary Fig. S2). It is thus possible that surface accessibility, due to the presence of an excess of HDA ligand in solution, hampers the access of the incoming metal to the Co-NRs surface. However, the

presence of HDA is necessary in order to guarantee a good dispersion of the nanorod seeds in solution. In order to overcome these obstacles, we have undertaken a surface modification of the bare Co-NRs by introducing a buffer layer that could remediate interfacial strain and/or surface chemistry issues responsible for the full-shell formation failure. [{$Sn(NMe_2)_2$}$_2$] can be reduced to metallic tin, which can form alloys with all three metals[36-38]. A buffer layer of gradient composition, in which the three elements are easily accommodated at the interface, could facilitate the development of a conformal metal shell[39]. Additionally [{$Sn(NMe_2)_2$}$_2$], acting as a ligand through the amide nitrogen, could displace the native laurate ligands present on the seed nanorod[5], which seem to hinder the interaction of the surface with the noble metal. Finally, Sn(II), can be reduced to Sn(0) or oxidized to Sn(IV) in redox reactions upon demand, during the different stages of the shell growth. Thus, Co-NRs were mixed with a [{$Sn(NMe_2)_2$}$_2$] solution and HDA and stirred at room temperature, in order for the tin compound to interact with the nanorod surface. [$AuClPPh_3$] was then added and the solution was heated under H_2. The Au growth step was repeated once (See Supplementary Information). Transmission Electron Microscopy (TEM) observations (Figure 1a) show that the resulting nano-objects do not present the same aspect as the one of Co-Au prepared under exactly the same conditions, but without [{$Sn(NMe_2)_2$}$_2$] (Supplementary Figure S1). Measurement of the nanorod dimensions before and after reaction indicates that growth of a thin shell of less than 1 nm thickness has taken place (dimensions are given in Methods). High resolution TEM (HRTEM) observations reveal the presence of a thin layer surrounding the Co-NR (Figure 1b). As expected, the Co core presents the same crystal structure as prior to shell growth. Despite the fact that the shell layer thickness is not uniform, it can be considered as monocrystalline since no grain boundaries are visible along the nanorod axis. The shell lattice parameters indeed correspond to Au which has grown epitaxially on the Co surface. The opportunity to add plasmonic properties to the hybrid nano-object incited us to try to

increase the layer thickness by repetitive Au depositions, which resulted in preferential Au growth on thicker shell areas, without however increasing significantly the thickness of the thinner areas (Supplementary Fig. S3). Whereas the positive effect of Sn on the Au shell growth is clear, the presence of Sn on the nanorods could not be observed by HRTEM experiments. In order to localize Sn and have an insight into the element distribution within the core-shell nanorods, Scanning Transmission Electron Microscopy-Energy Dispersive X-ray (STEM-EDX) experiments have been performed on isolated nano-objects by using a ChemiSTEM detector (Figure 1c-f). From these images we can clearly see that Au is forming a shell containing a small amount of Sn, and there is no indication that Sn presence is limited to a layer between Co and Au.

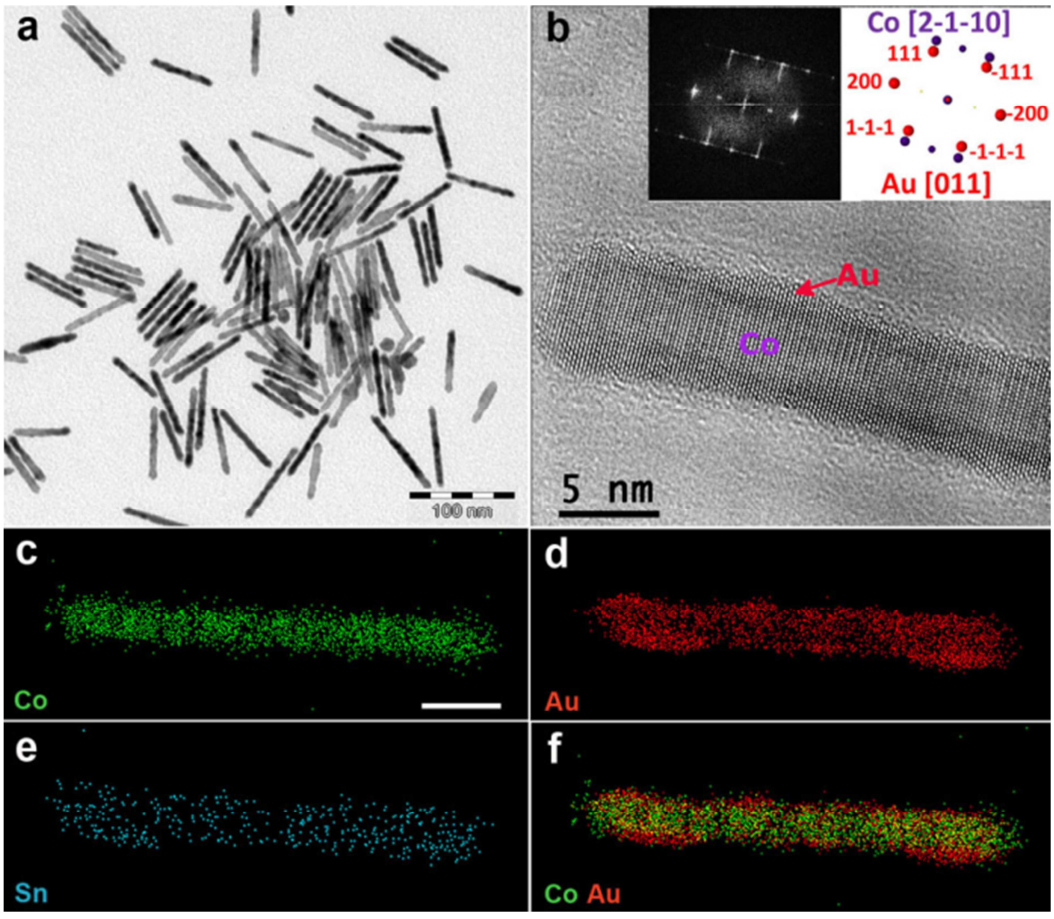

Figure 1. Co@SnAu nanorods. a, Low magnification TEM image (scale bar: 100 nm). **b**, HRTEM image of a Co@SnAu nanorod, showing the core@shell structure. In the inset we present the Fast Fourier Transform (FFT) on the whole image showing the epitaxial relationships between the two lattices (scale bar: 5 nm). The epitaxial relationship between Co and Au is as follows: Co[2-1-10](01-10) // Au[110](110). It means that the interfacial plane is parallel to the (01-10) Co plane and (110) Au plane. The lattice misfit based on lattice site coincidence relationships is 0.5% considering the interreticular distances $d_{2\text{-}1\text{-}10}$ for Co and d_{220} for Au, and -2.7% with d_{0001} for Co and d_{200} for Au. . **c-f**, STEM-EDX maps showing the elemental distribution separately (c-e), and from the pair Co-Au (f) (Co: green, Au: red, Sn: blue). Scale bar for all EDX maps is 10 nm.

Treatment of the Co-NRs with $[\{Sn(NMe_2)_2\}_2]$ followed by three successive Pt deposition steps (See Materials and Methods), leads to the nanorods shown in Figure 2. A careful observation of the TEM images shows that most of the nanorods are covered by a layer Figure 2a. However not all of them are uniformly coated. We can distinguish specimens of variable shell thickness and nanorods that appear not to be covered at all, indicated by red and blue arrows respectively. Supplementary Pt depositions increase the existing thickness difference between covered and uncovered areas (Supplementary Fig. S4). Obviously, once the first layers of Pt deposited, the additional Pt preferentially deposits on the already Pt-covered areas. HRTEM studies (Figure 2b) show that Pt also grows epitaxially on the nanorod surface. The STEM-EDX measurements performed on fully covered isolated nanorods (Figure 2c-f) showed that a smooth Pt-containing shell is present. Again, the presence of Sn does not appear to be strictly limited to a layer between Co and the noble metal, and there is no evidence of a metallic Sn crystal lattice.

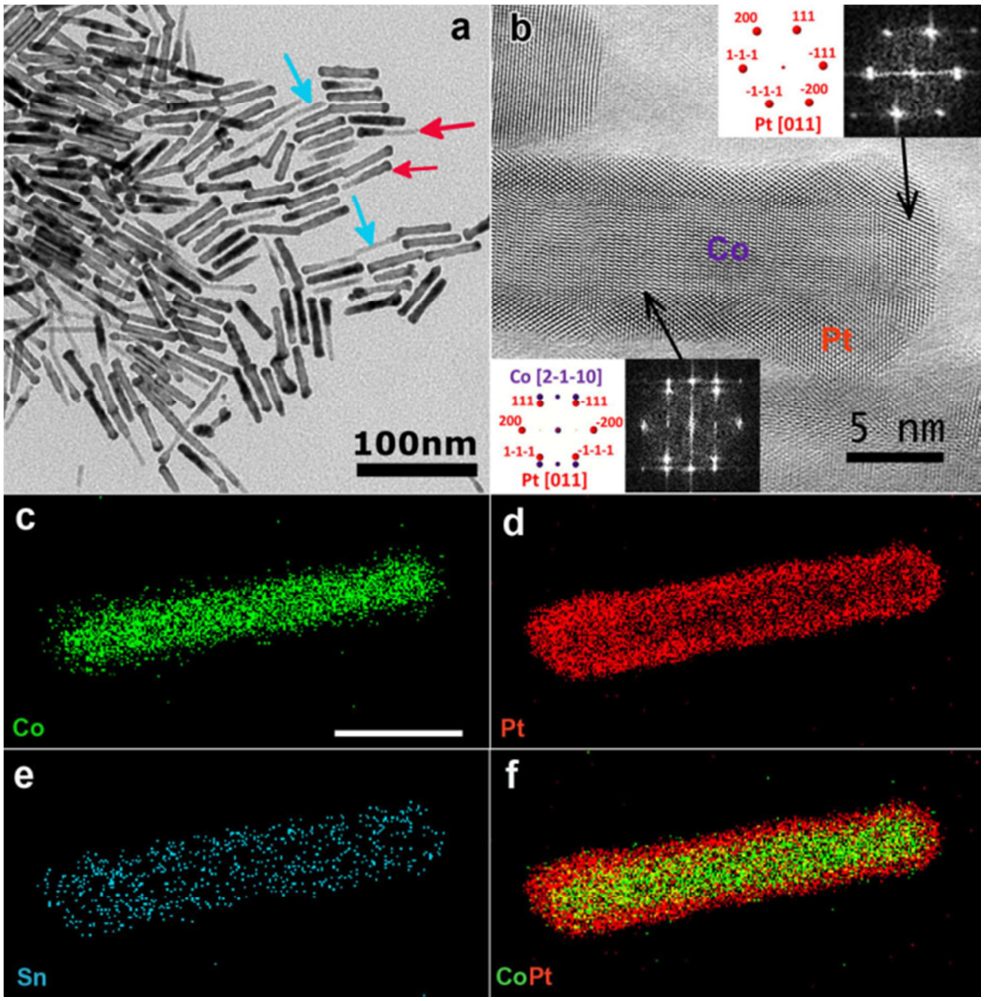

Figure 2. Co@SnPt nanorods. a, Low magnification TEM image of Co@SnPt nanorod sample. The red arrows indicate rods where Co is not completely covered by the shell. Blue arrows indicate nanorods for which no shell can be discerned. **b**, HRTEM image of an isolated nanorod. In the insets we present FFTs of the areas indicated by the arrows. The growth orientation is different on the lateral sides and on the tips. The epitaxial relationship between Co and Pt on the lateral sides is Co[2-1-10](01-10) // Pt[110](110) and on the tips Co[2-1-10](0001) // Pt[110](111). For the lateral sides, the interfacial plane is parallel to the (01-10) Co plane and (110) Pt plane. The lattice misfit based on lattice site coincidence

relationships is -3.45% considering the interreticular distances $d_{2\text{-}1\text{-}10}$ for Co and d_{220} for Pt, and -6.75% with d_{0001} for Co and d_{200} for Au. **c-f**, STEM- EDX maps showing the distribution of each element separately as well as of the couple CoPt on an isolated nanorod, which has a completely covered Co core (Co: green, Pt: red, Sn: blue). Scale bar for all EDX maps is 10nm.

The resistance of the Co@SnAu and Co@SnPt nanorods to water has been tested by TEM observation on the samples after exposing them to the air, adding distilled water to core-shell powders and leaving them in water for 2 days (Supplementary Fig. S5). Water affects the Au- and Pt-coated nanorods differently. Almost all Co@SnAu nanorods were severely attacked, but fully coated Co@SnPt specimens are seemingly unaffected by water. Nevertheless, incompletely covered or naked rods appear corroded. From the TEM/HRTEM images of the sample prior to water exposure, all Co@SnAu nanorods (Figure 1) appear to be coated in a similar manner. However, important variations of the shell thickness along their length can be observed and, at some points the shell is very thin (2 or 3 atomic layers). We presume that thinner Au shell areas are more reactive and prone to etching. The Pt shell (Figure 2) is much thicker and smoother, presenting fewer shell thickness variations. The fully covered nanorods remain intact after water exposure, but incompletely covered nanorods are corroded.

These results prompted us to use Pt and Au successively. The idea was to use these two metals of limited miscibility[40], in order to avoid extended overgrowth of the second noble metal on areas already occupied by the first metal, thus favoring deposition on uncovered Co areas. In Figure 3 we present the core-shell nanorods prepared by three successive steps: (i) $[\{Sn(NMe_2)_2\}_2]$ treatment of the Co-NRs, (ii) 3 cycles of Pt deposition and (iii) 2 cycles of Au deposition (See Supplementary Information). A TEM image of the Co@SnPtAu nanorods is shown in (Figure 3a). A less smooth surface in comparison to the Co@SnAu and Co@SnPt nanorods is observed. The HRTEM image presented in Figure 3b shows the presence of a

polycrystalline shell, while STEM-EDX measurements (Figure 3c-f) revealed that indeed, Pt and Au are complementary as shown further in Supplementary Fig.S6. It is important to point out that these nanorods are not affected by water as is demonstrated by the TEM image showing a sample of Co@SnPtAu nanorods after 2 days exposure to water (Supplementary Fig. S7).

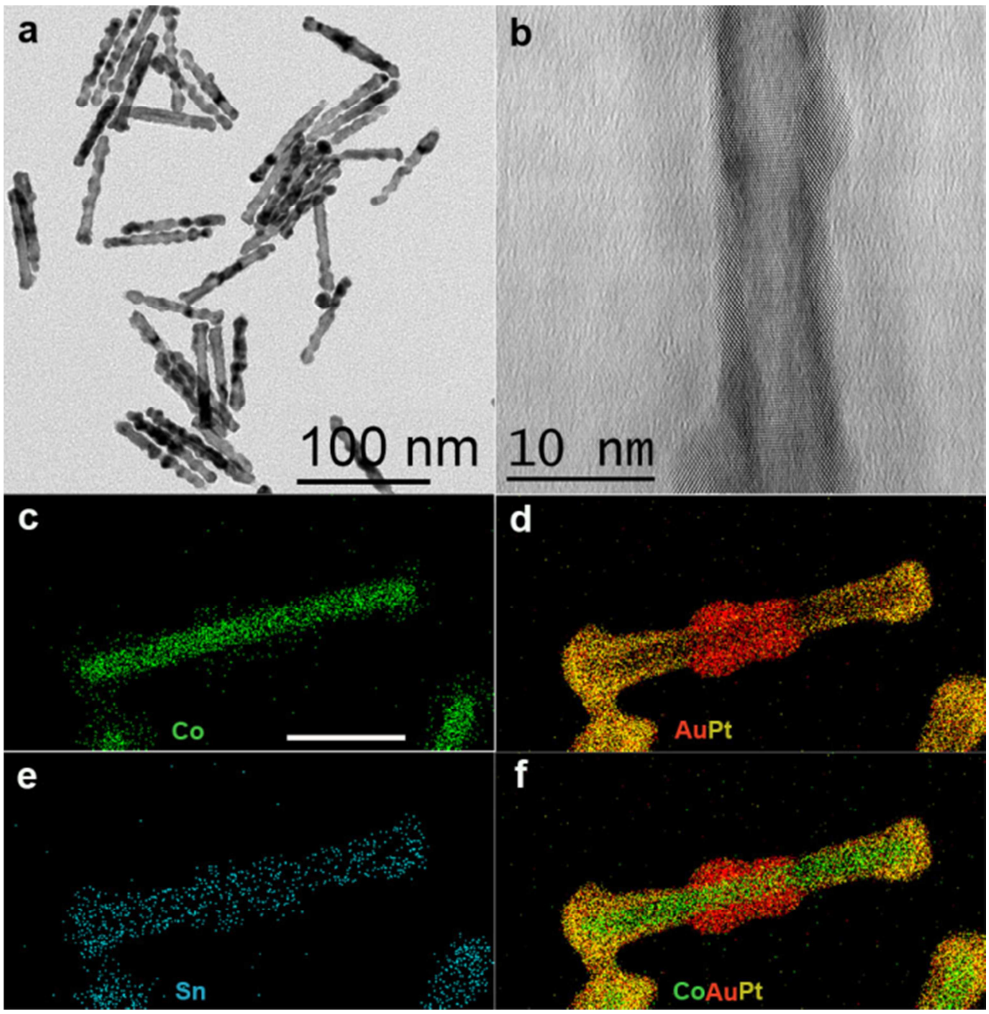

Figure 3. **Co@SnPtAu nanorods. a**, Low magnification TEM image of a Co@SnPtAu nanorod sample (scale bar: 100 nm). **b**, HRTEM image on an isolated nanorod, revealing the polycrystalline nature of the shell (scale bar: 10 nm). **c-f**, STEM- EDX maps showing the

location of the elements on a fully covered nanorod (c: Co, d: Au and Pt, e: Sn;, f: Co, Au and Pt. (Co: green, Sn: blue, Au: red Pt: yellow). Scale bar for all EDX maps is 20nm.

In order to better understand the structure of the core-shell nano-objects, X-Ray absorption spectroscopy (XAS) measurements were performed on Co@SnM (M= Au and/or Pt) samples and the results are presented in Figure 4. The Co K-edge X-ray Absorption Near Edge Structure (XANES) spectra for all samples and the reference are presented in Figure 4a. Together with Supplementary Table S1 these results show that in all samples Co is metallic. The corresponding XANES spectra for the Sn, Au and Pt edges are presented in Supplementary Tables S2-S4 and Supplementary Figs. S8-S10. The coordination numbers and bond distances were determined from the Extended X-Ray Absorption Fine Structure (EXAFS) data of Figure 4b-d and in Supplementary Table S5 and Suplementary Figs. S11-S13). This investigation revealed that all samples contain only zero-valent Co, Pt and Au. No Pt-Au alloy was detected by XAS in the Co@SnPtAu sample. However, Sn forms an alloy with Pt in both Co@SnPt and Co@SnPtAu samples. Interestingly for the Co@SnAu sample Sn is not metallic and it seems to be bonded to 4 lighter scatterers (O or N) (Supplementary Fig. S12).

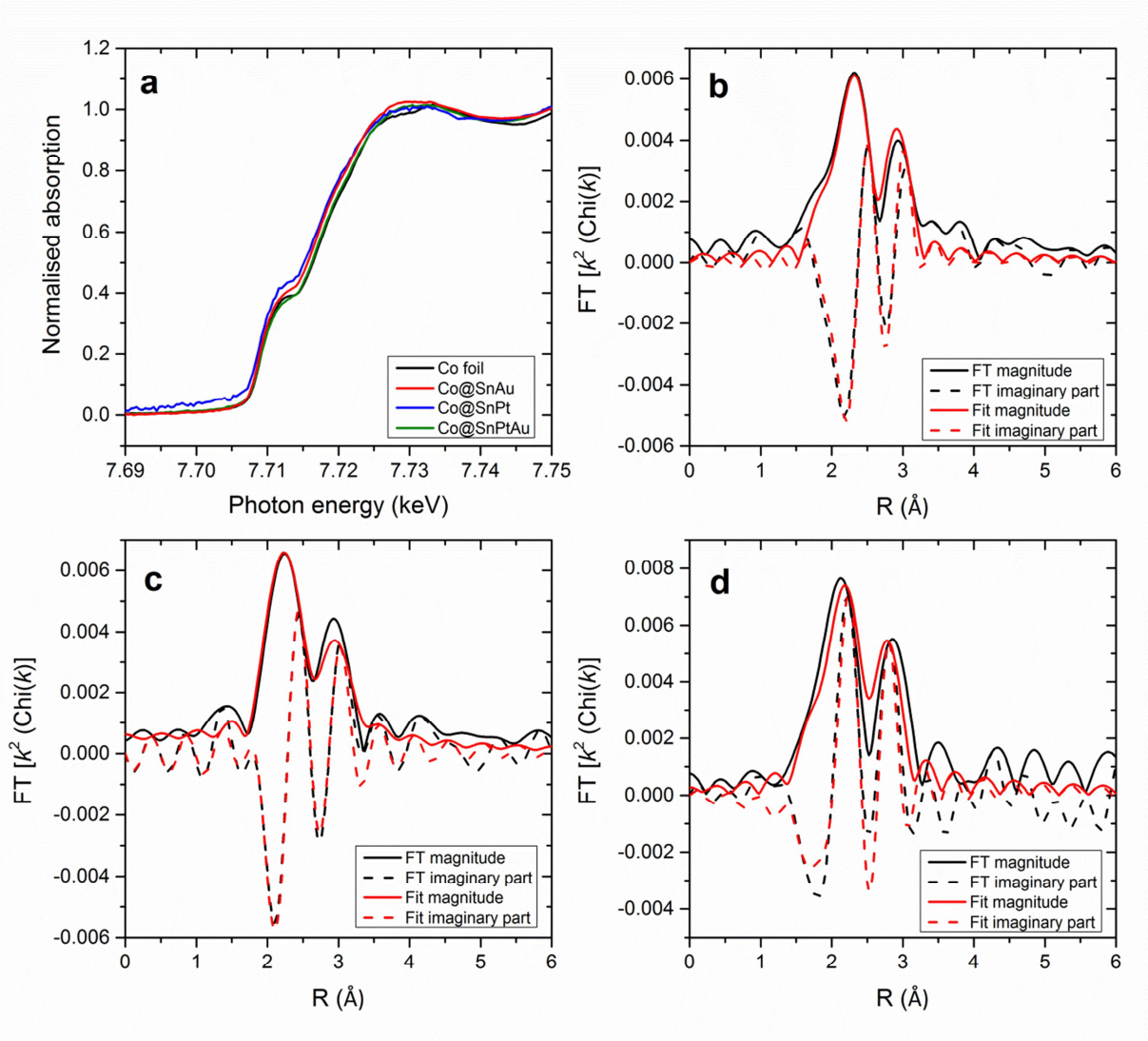

Figure 4. XAS measurements on core-shell nanorods. **a**, XANES Co K-edge spectra of samples and Co-foil reference. **b**, Au L_3-edge R space EXAFS fitting result of Co@SnAu. k^2: Δk = 2.6-10.5 $Å^{-1}$ proving that Au is metallic and not alloyed. The EXAFS of Co@SnPtAu was similar. **c**, Pt L_3-edge R space EXAFS fitting result of Co@SnPt. k^2: Δk = 2.7-9.2 $Å^{-1}$, proving that Pt is metallic. The EXAFS of Co@SnPtAu was similar. **d**, Sn K-edge R space EXAFS fitting result of Co@SnPt). k^2: Δk = 2.7-10.2 $Å^{-1}$. The EXAFS at the Sn edge does not correspond to Sn metal and instead is indicative of Sn-Pt scattering only. This means that the Sn has formed an alloy with Pt.

Sn is the crucial factor that enables the noble metal shell development. Thus, in a first approach we used TEM to examine the Co-NRs after treatment with $[\{Sn(NMe_2)_2\}_2]$ and washing with toluene. As in the case of the Co@SnM nanorods, only STEM-EDX analysis allows Sn detection, indicating that an amorphous layer covers the Co-NRs (Supplemenatry Fig.S14). X-ray photoelectron spectroscopy (XPS) measurements on a Co@Sn sample after washing confirm the metallic nature of Co[41]. Furthermore they show that part of tin is Sn^0 but the major part is Sn^{2+} associated to O (SnO), which presumably originates from the Co-seed native laurate ligands (Sn^{2+}/Sn^0 = 3.2). The presence of a small percentage of Sn-N bonds cannot be excluded. Since no H_2 has been used during treatment with $[\{Sn(NMe_2)_2\}_2]$, and HDA is not able to reduce $[\{Sn(NMe_2)_2\}_2]$ at room temperature, the presence of metallic Sn is probably due to a limited galvanic displacement reaction between Co(0) and Sn(II) at the Co/Sn interface (for XPS details see Supplementary Table S6 and Supplementary Fig. S15)

Thus, Sn treatment seems to influence two parameters that dominate the reaction outcome. $[\{Sn(NMe_2)_2\}_2]$ acts as a metal-containing ligand that "wets" the entire Co surface, presumably by displacing, or reacting with existing ligands of the Co surface. This effect could account for its positive role on the conformal shell formation independently of the shell-metal used. Whereas the exact nature of the Sn species present on Co@Sn intermediate is elusive, it is possible that upon contact with Co-NRs, a small amount of the $[\{Sn(NMe_2)_2\}_2]$, not detectable by XAS but visible by XPS, is reduced in a transmetallation reaction, but most of the Sn is non-metallic. Subsequent reaction with $[PtMe_2COD]$ under H_2 reduces both Pt and Sn which form a continuous shell of Pt-Sn alloy, allowing a reduction the interfacial energy between Co and Pt. Subsequent $[AuClPPh_3]$ reduction takes place mainly on Pt deficient areas. On the other hand, Sn is practically non-metallic in Co@SnAu. This difference could be due to the Pt acting as an efficient hydrogenation catalyst in the cases of Co@SnPt and Co@SnPtAu.

While the above experiments give an indication about the coating efficiency of the SnPtAu shell, the *sine qua non* condition for nanorod implementation in an aqueous environment is the conservation of the Co-core magnetic properties. Thus, magnetic measurements were performed on the water-resistant Co@SnPtAu before and after exposure of the sample (i) to air and (ii) to water (Figure 5). For comparison, Co-NRs were also measured following the same experimental protocol (See Methods). Before any exposure to air or water, both samples present a magnetization at saturation very close to the expected bulk value (M_S=160 Am^2/kg and 158 Am^2/kg at T = 4 K for Co-NRs and Co@SnPtAu respectively). The absence of exchange bias (EB) after field cooling (FC) under a 5T magnetic field (see Figure 5a and in Supplementary Table S7) corroborates the metallic character of the Co core, and means that coating does not affect M_S. Moreover, the high coercive field (H_C = 0.71 T at 4 K), of the Co@SnPtAu nanorods (just below the one of Co-NRs), confirms that their effective magnetic anisotropy is high enough (> 4 10^5 J/m^3) for applications in which hard magnetic materials are required. As expected, the Co-NRs present several obvious signs of oxidation after 5 days exposure to the air: a large drop of M_S and of H_C, and a high exchange bias field H_{EB} ~ 0.5 T (see Figure 5b). On the contrary, the magnetization of Co@SnPtAu nanorods does not seem to be sensitive to the exposure to the air after 6 days. The samples exposed to the air, were then immersed into distilled water for 1 day. Whereas the oxidation unambiguously advanced in the case of Co-NRs, the Co@SnPtAu nanorods only displayed slight changes of their magnetic properties. At T = 300 K, their magnetization was still high but decreased from M_S = 153 Am^2/kg (before water exposure) to M_S = 138 Am^2/kg. Interestingly, the magnetization decrease was less pronounced at low temperature (M_S = 153 Am^2/kg), at which 97 % of the initial M_S value, and a small exchange bias field H_{EB} = 7 mT were measured. The Co@SnPtAu nanorods were then subjected to an extended conditioning period, first to the air for 3 months, and subsequently to water for 5 days, giving rise to a monotonous decrease of

M_S (91% and 74% of the initial M_S value at 4 K and 300 K respectively). However this decrease was much less severe than in the case of Co-NRs (24% and 21% at 4 K and 300 K respectively). This very limited oxidation could be due to the fact that some imperfectly covered areas are still remaining. Despite the drop of 26% of M_S at 300 K, the Co@SnPtAu nanorods still present a high M_S (~115 Am^2/kg) and a coercive field large enough (0.60 T at 4 K and 0.34 T at 300 K) for applications requiring both high Ms and a hard magnetic behavior.

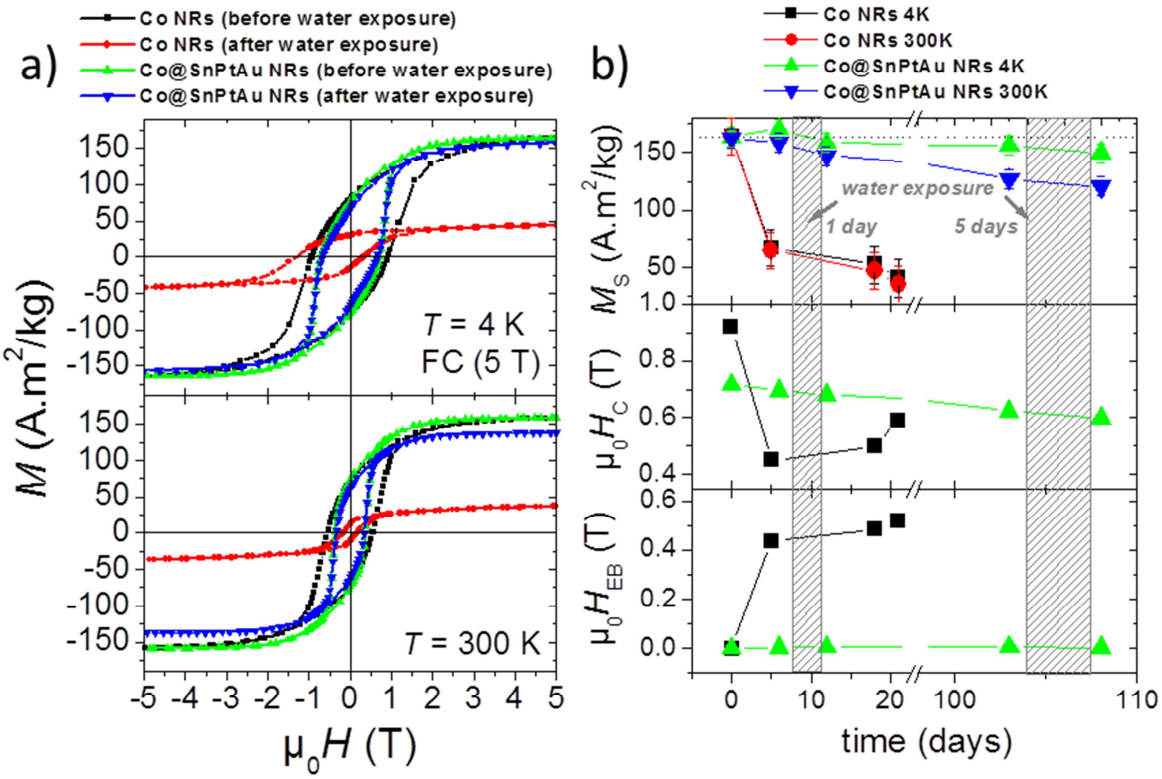

Figure 5. Magnetic properties of Co@SnPtAu vs Co-NRs. a, Hysteresis loops measured at T = 4 K, and T = 300 K after field cooling (FC) under 5 T of Co-NRs (black squares: before water exposure; red squares: after water exposure) and Co@SnPtAu nanorods (green triangles: before water exposure; blue triangles: after water exposure). **b**, time evolution of the saturation magnetization (Ms) (top), coercive field (Hc) (middle), and exchange bias field

(H_{EB}), defined as $H_{EB} = (H_{C+} - H_{C-})/2$ with H_{C+} and H_{C-} the positive and negative coercive field respectively (bottom). The Co-NRs traces at 4 K correspond to the black squares, and at 300 K to the red circles. Co@SnPtAu nanorod traces at 4 K correspond to the green triangles, and at 300 K to the blue triangles. The shaded areas indicate the time interval during which the nanorods have stayed in contact with water (1 and 5 days). During the time interval between the two water-exposure treatments the samples were exposed to the air.

To our knowledge, non-oxide magnetic nano-objects of both high Ms and anisotropic shape have not been reported. Indeed, existing ferromagnetic oxide nanorods, which can be used in water, have much lower Ms than Co@SnPtAu nanorods[42,43]. On the other hand, the existing nano-objects of high Ms are either not resistant towards oxidation or isotropically shaped[10,11,44].

We have achieved the first successful synthesis of air and water-resistant highly magnetic and ferromagnetic nanorods through treatment of Co-NRs with $[\{Sn(NMe_2)_2\}_2]$. This treatment can modify the surface chemistry of Co-NRs enabling the subsequent development of a conformal noble metal shell which renders them air- and water-resistant. While the present work is mainly focused on a specific metal, this new chemical approach has a broad interest and can be adapted to the synthesis of core-shell nanoparticles of different shapes and compositions with applications spanning from nanomedicine to ferrofluids and catalysis.

Methods

Due to the air sensitivity of the metal precursors, as well as of the Co-NRs, all experiments were performed under inert conditions, in the interior of a glove-box or by using standard Schlenk techniques. The starting Co-NRs have been prepared by slight modifications of an already published procedure[5]. The naked Co-NRs were treated with $[\{Sn(NMe_2)_2\}_2]$ before coating by the noble metals takes place. A detailed description of the standard procedures is given in the Supplementary Information.

The dimensions of the samples presented in Figures 1-3 are given below.

Co@SnAu: Sample shown in Figure 1. Before coating: length (L) = 61±6nm, diameter (d) = 5.7±0.7 nm; after coating: L = 61± 5 nm, d = 7.2±0.7nm EDX analysis on several areas of a TEM grid yields the following mean values % at: Co = 67%, Sn = 10%, Au = 23%.

Co@SnPt: The size distribution taking into account only the fully covered nanorods indicates that the shell thickness is about 1 nm. Sample shown in Figure 2: Before coating: L = 44±4 nm, d = 5.7± 0.5 nm; after coating: L = 46±3 nm, d = 7.7± 0.6 nm

EDX analysis on several areas of a TEM grid yields the following mean values % at: Co = 52%, Sn = 6%, Pt = 42%

Co@SnPtAu: The mean length and diameter of the final nanorods have increased, however the irregular metal deposition does not allow a reliable and statistically relevant diameter measurement Sample shown in Figure 3: naked nanorods: L = 74±5 nm, d = 5.9± 0.5 nm; core-shell nanorods: L = 75±6 nm, d: around 9 nm. EDX analysis on several areas of a TEM grid yields the following mean values % at: Co = 35%, Sn = 4%, Pt = 40% Au = 21%.

TEM-HRTEM

Samples for TEM observations were prepared in a glove box, by drop-casting toluene suspensions of the nanorods on a carbon coated copper grid.

TEM characterization was performed on a JEOL JEM 1011 microscope, equipped with a W thermionic electron source and a Mega-View Olympus CCD camera and working at an acceleration voltage of 100 kV, or with a JEOL JEM 1400 microscope equipped with LaB6 thermionic electron source and working at an acceleration voltage of 120 kV. HRTEM observations were realized using a 200 kV FEI Tecnai microscope equipped with a field emission gun and a Cs corrector which avoids delocalization effects at interfaces (point resolution of 0.12 nm). The structural features of the nanostructures imaged by HREM were studied by means of 2D Fourier analysis.

STEM-EDX

STEM-EDX measurements were performed using an aberration-corrected cubed FEI-Titan 60-300 electron microscope operated at 200kV. For the acquisition of the maps, a ChemiSTEM system was used[45]. For the acquisition and quantification of the maps, the ESPRIT software was used.

Routine EDX was performed using JEOL JEM 2100F electron microscope equipped with a field emission gun (FEG) and SDD Brucker (light elements detection), with a resolution of 127eV.

XAS

X-ray absorption measurements were acquired at the Co K-edge (7.709 keV), Sn K-edge (29.200 keV), Pt L_3-edge (11.564 keV) and Au L_3-edge (11.919 keV) on the bending magnet beam line of the Materials Research Collaborative Access Team (MRCAT) at the Advanced Photon Source, Argonne National Laboratory. The data were collected in transmission step-scan mode. Photon energies were selected using a water-cooled, double-crystal Si (111) monochromator, which was detuned by approximately 50 % to reduce harmonic reflections.

The ionization chambers were optimized for the maximum current with linear response (~10^{10} photons detected/sec) with 10 % absorption in the incident ion chamber and 70 % absorption in the transmission X-ray detector. The appropriate metal foil spectrum was acquired simultaneously with each sample measurement for energy calibration.

Nanorod samples after being washed and dried were pressed into a cylindrical sample holder consisting of six wells, forming a self-supporting wafer. All samples were prepared in a N_2 glove box and the sample holder was placed in a quartz tube (1–in. OD, 10–in. length) sealed with Kapton windows by two Ultra-Torr fittings. Samples of interest were pressed directly as received to achieve an absorbance (μx) of approximately 1.0.

Standard data reduction techniques were employed to fit the data using the WINXAS 3.1 software program. The normalized, energy–calibrated absorption spectra were obtained using standard methods. The edge energy was determined from the maximum of the first peak of the first derivative of the XANES spectrum. For the Co, Pt, Au edges experimental phase shift and backscattering amplitudes were measured using the appropriate metal foils (coordination numbers and bond distances shown in Supplementary Table S5). For the Sn edge, SnO_2 was used as the reference for Sn bonded to a light scatterer (Sn-O or Sn-N scattering). The EXAFS and XANES of the $[Sn(N(CH_3)_2]_2$ precursor was also obtained for comparison. Since experimental references were not available for alloys, theoretical references were prepared for Sn-Co and Sn-Pt using FEFF. The EXAFS parameters were obtained by a least square fit in *R*-space of the k^2-weighted Fourier Transform (FT) data for all samples except the Sn K-edge of sample Co@SnAu where the EXAFS parameters were obtained by a least square fit in *k*-space of the k^2-weighted Back-Fourier Transform data. The Debye-Waller factor ($\Delta\sigma^2$) is dependent on the amount of disorder in the sample and was fixed at a given edge at either 0.001 or 0.002 for metallic particles or 0.004 for light scatterers. All fits were single shell.

XPS

XPS measurements were carried out with a Thermo Scientific K-Alpha X-ray photoelectron spectrometer, using a focused monochromatized Al Kα radiation (hν = 1486.6 eV). The XPS spectrometer was directly connected through a glove box under argon atmosphere, in order to avoid moisture/air exposure of the samples. For the Ag 3d5/2 line the full width at half-maximum (FWHM) was 0.50 eV under the recording conditions. The X-ray spot size was 400 μm. Peaks were recorded with constant pass energy of 20 eV. The pressure in the analysis chamber was less than 2×10^{-8} Pa. Short acquisition time spectra were recorded at the beginning and at the end of each experiment to check that the samples did not suffer from degradation during the measurements. Peak assignments were made with respect to reference compounds analyzed in the same conditions. The binding energy scale was calibrated from the hydrocarbon contamination using the C 1s peak at 285.0 eV. Core peaks were analyzed using a nonlinear Shirley-type background[46]. The peak positions and areas were optimized by a weighted least-squares fitting method using 70% Gaussian, 30% Lorentzian line shapes. Quantification was performed on the basis of Scofield's relative sensitivity factors[47]. Several XPS analyses were performed at different positions to make the results statistically reliable.

Magnetic measurements

The magnetic properties of Co and Co@SnPtAu nanorods have been characterized by VSM using a 9T EverCool II Quantum Design PPMS.

In order to ensure a reliable quantitative analysis of the magnetization evolution upon air and water exposure, the same sample was used throughout the whole series of measurements, thus avoiding any errors stemming from the use of different samples. Standard VSM capsules were filled with a known amount (a few mg) of sample and sealed, without any other material commonly used to freeze the magnetic compound (vacuum grease, epoxy…). The addition of

the blocking material (vacuum grease, epoxy…) would prevent contact of the nanorods with air and water.

The initial magnetization is measured for both Co-NRs and Co@SnPtAu, freshly synthesized samples, kept in the glove box. To avoid any oxidation, the samples are prepared in the glove-box, and transferred to the cryostat in a Schlenck vessel. The VSM capsule containing the sample is rapidly introduced into the VSM in order to avoid exposure of the sample to the air. These measurements represent the reference of the air/water-stability of the nanorods and are referred as "t = 0" (see Figure 5). Zero Field Cooled (ZFC) and Field Cooled (FC) at 5T measurements are realized at 4 K in order to confirm the metallic state of the Co before water addition. ZFC was performed by cooling the sample down to 4 K without application of magnetic field and field-dependent magnetization was recorded at 4 K. The temperature was then increased to 300K, and a 5T magnetic field was applied. A second field- dependent magnetization was recorded after having cooled down to 4K while the 5T magnetic field was applied. The mass magnetization of Co is calculated by taking into account the metallic fraction of Co obtained by ICP.

After measuring the magnetic properties before air and water exposure, the VSM capsules were opened to the air and after measurement of the effect of air exposure, they were completely filled with deionized water (around 40 µL). After the complete evaporation of the water, ZFC FC measurements were performed again. We emphasize that only this protocol that measures the same samples before and after exposure allows a quantitative analysis and control of the variation of the magnetization of the sample after exposure.

Acknowledgements

The authors thank the European Commission for the FP7 NAMDIATREAM project (EU NMP4-LA-2010-246479), the European Commission and the Région Midi-Pyrénées for the POCTEFA Interreg project (MET-NANO EFA 17/08) and the French Research National Agency (ANR) for the project CARMA (ANR-09-BLAN-0804). This study has been partially supported through the grant NEXT n° ANR-10-LABX-0037 in the framework of the "Programme des Investissements d'Avenir" and has received funding from the European Union Seventh Framework Programme under Grant Agreement 312483 - ESTEEM2 (Integrated Infrastructure Initiative–I3). TEMSCAN service is acknowledged for the routine TEM and EDX. G.V.T. and S.B. acknowledge financial support from European Research Council (ERC Advanced Grant # 24691-COUNTATOMS, and ERC Starting Grant # 335078-COLOURATOMS). X-ray absorption spectroscopy studies by JTM and JRG were supported by the Institute for Atom-efficient Chemical Transformations (IACT), an Energy Frontier Research Center funded by the US Department of Energy, Office of Science, Office of Basic Energy Sciences. Use of the Advanced Photon Source is supported by the U.S. Department of Energy, Office of Science, and Office of Basic Energy Sciences, under Contract DE-AC02-06CH11357. MRCAT operations are supported by the Department of Energy and the MRCAT member institutions.

Author contribution

S.L-M and B.C. performed the synthesis of the nanorods, optimized the procedures and performed routine TEM observations, R.P.T. and M.R. performed the magnetic measurements and analyzed the results, C.G-M., T.H. performed EDX and HRTEM observations and participated to the result analysis, P-F.F. and C.G. trained C.G-M. and T.H. and analyzed EDX and HRTEM results T.A., S.B. and G.V.T. are responsible for the acquisition and analysis of the STEM-EDX data. H.M. performed the XPS experiments and interpreted the

results, K.S. was responsible of the nanorod synthesis, trained S.L-M. and B.C. and wrote the paper with the participation of all authors.

The authors declare no competing financial interests

References

1. Sun, S., Murray, C.B., Weller, D., Folks, L. & Moser, A. Monodisperse FePt Nanoparticles and Ferromagnetic FePt Nanocrystal S. *Science* **287,** 1989-1992 (2000).

2. Frey, N. A., Peng, S., Cheng, K. & Sun, S. Magnetic Nanoparticles: Synthesis, Functionalization and Applications in Bioimaging and Magnetic Energy Storage. *Chem. Soc. Rev.* **38,** 2532-2542 (2009).

3. Lu, A-H., Salabas, E.L. & Schlüth, F. Magnetic nanoparticles: Synthesis, protection, Functionalization and Application. *Angew. Chem. Int. Ed.* **46,** 1222-1244 (2007).

4. Ho, D., Sun, X. & Sun, S. Monodisperse Magnetic Nanoparticles for Theranostic Applications. *Acc. Chem. Res.* **44,** 875-882 (2011).

5. Wetz, F., Soulantica, K., Respaud, M., Falqui, A. & Chaudret, B. Synthesis and magnetic properties of Co nanorod superlattices. *Mater. Sci. Eng. C* **27**, 1162-1166 (2007).

6. Soulantica, K. *et al.* Magnetism of single-crystalline Co nanorods. *Appl. Phys. Lett.* **95**, 152204 (2009).

7. Guftleich, O. *et al*. Magnetic Materials and Devices for the 21st Century: Stronger, Lighter, and More Energy Efficient. *Adv. Mater.* **23,** 821-842 (2011).

8. Thurn-Arbrecht *et al*. Ultrahigh-Density Nanowire Arrays Grown in Self-Assembled Diblock Copolymer Templates. *Science* **290**, 2126-2129 (2000).

9. Peng, S. Wang, C., Xie, J. & Sun, S. Synthesis and Stabilization of Monodisperse Fe Nanoparticles *J. Am. Chem. Soc*. **128,** 10676-10677 (2006).

10. Yoon, T-J., Lee, H., Shao, H. & Weissleder, R. Highly Magnetic Core-Shell Nanoparticles with a Unique Magnetization Mechanism. *Angew. Chem. Int. Ed.* **50,** 4663-4666 (2011).

11. Seo, W.S. *et al*. FeCo/graphitic-shell Nanocrystals as Advanced Magnetic-Resonance-Imaging and Near-Infrared Agents. *Nature Mater*. **5,** 971-976 (2006).

12. Levin, C.S. *et al*. Magnetic-Plasmonic Core-Shell Nanoparticles. *ACS Nano* **3,** 1379-1388 (2009).

13. Fan, Z., *et al*. Multifuctional Plasmonic Shell-Magnetic Core nanoparticles for Targeted Diagnostics, Isolation, and Photothermal destruction of Tumor Cells. *ACS Nano* **6,** 1065-1073 (2012).

14. Elghanian, R., Storhoff, J. J., Mucic, R. C., Letsinger, R. L. & Mirkin, C. A. Selective Colorimetric Detection of Polynucleotides Based on the Distance-Dependent Optical Properties of Gold Nanoparticles. *Science* **277,** 1078-1081 (1997).

15. Guo, S., Zhang, S. & Sun, S. Tuning Nanoparticle Catalysis for the Oxygen Reduction Reaction. *Angew. Chem. Int. Ed.* **52,** 8526-8544 (2013). (8526)

16. Sasaki, K. *et al*. Core-Protected Platinum Monolayer Shell High-Stability Electrocatalysts for Fuel-Cell Cathodes. *Angew. Chem. Int. Ed.* **49,** 8602-8607 (2010). (8602)

17. Liu, Y., Li, D. & Sun, S. Pt-based Composite nanoparticles for Magnetic, Catalytic, and Biomedical Applications. *J. Mater. Chem.* **21,** 12579-12587 (2011).

18. Chaudhuri, R.G. & Paria, S. Core/Shell Nanoparticles : Classes, Properties, Synthesis Mechanisms, Cheracterization, and Applications *Chem. Rev*. **112,** 2373-2433 (2012).

19. Habas, S. E., Lee, H., Radmilovic, V. & Somorjai, G. A. , Yang, P. Shaping Binary Metal Nanocrystals Through Epitaxial Seeded Growth. *Nature Mater.* **6,** 692-697 (2007).

20. Min, Y., Kwak, J., Soon, A. & Jeong, U. Nonstoichiometric Nucleation and Growth of Multicomponent Nanocrystals in Solution. *Acc. Chem. Res*. DOI:10.1021/ar500133w (2014).

21. Carbone, L. & Cozzoli, P.D. Colloidal Heterostructured Nanocrystals: Synthesis and Growth Mechanisms. *NanoToday* **5,** 449-493 (2010).

22. Feng, Y., *et al*. An Unconventional Role of Ligand in Continuously Tuning of Metal-Metal Interfacial Strain *J. Am. Chem. Soc*. **134,** 2004-2007 (2012).

23. Lee, W. *et al*. Redox-Transmetalation Process as a Generalized Synthetic Startegy for Core-Shell Magnetic Nanoparticles *J. Am. Chem. Soc*. **127,** 16090-16097 (2005).

24. Lu, Z. *et al*. Magnetic Switch of Permeability for Polyelectrolyte Microcapsules Embedded with Co@Au Nanoparticles. *Langmuir* **21,** 2042-2050 (2005).

25. Bao, Y. Calderon, H. & Krishnan, K.M. Synthesis and Characterization of Magnetic-Optical Co-Au Core-Shell Nanoparticles. *J. Phys. Chem. C* **111,** 1941-1944 (2007).

26. Schrittwieser, S. *et al*. Modeling and Development of a Biosensor Based on Optical Relaxation Measurements of Hybrid Nanoparticles. *ACS Nano* **6,** 791-801 (2012).

27. Liakakos, N. *et al*. Solution Epitaxial Growth of Cobalt Nanowires on Crystalline Substrates for Data Storage Densities Beyond 1Tbit/in^2. *Nano Lett.* **14,** 3481-3486 (2014).

28. Mertelj, A., Lisjak, D., Drofenik, M. & Copic, M. Ferromagnetism in Suspensions of Magnetic platelets in Liquid Crystal. *Nature* **504**, 237-241 (2013).

29. Salgueirino-Maceira, V., Liz-Marzán, L. & Farle, M. Water-Based Ferrofluids from Fe*x*Pt1-*x* Nanoparticles Synthesized in Organic Media. *Langmuir* **20,** 6946-6950 (2004).

30. Soulantika A. Lentijo-Mozo, S., Hungria-Hernansez, M-T., Tan, R.P. & Gatel, C. Magnetic Nano-Objects Covered with a Metallic Envelope. Patent N° WO/2014 102496.

31. Shylesh, S., Schünemann, V. & Thiel, W.R. Magnetically Separable Nanocatalysts: Bridges Between Homogeneous and Heterogeneous Catalysis. *Angew. Chem. Int. Ed.* **49,** 3428-3459 (2010).

32. Rossi, L.M., Costa, N.J.S., Silva, F.P. & Wojcieszak, R. Magnetic Nanomaterials in Catalysis: Advanced Catalysts for Magnetic Separation and Beyond. *Green Chem*. **16**, 2906-2933 (2014).

33. Wetz, F. *et al*. Hybrid Co-Au nanorods: Controlling Au Nucleation and Location**.** *Angew. Chem. Int. Ed***., 46,** 7079-7081(2007).
34. Markov, I.V. Crystal Growth for Beginners. Ch 4. (World Scientific Publishing Co. 2003)

35. Peng, Z. & Yang, H. Designer Platinum Nanoparticles: Control of Shape, Composition in Alloy, Nanostructure and Electrocatalytic Property. *Nano Today* **4,** 143-164 (2009).

36. Kanatzidis, M.G., Pöttgen, R. & Jeitschko, W. The Metal Flux: A Preparative Tool for the Exploration of Intermetallic Compounds. *Angew. Chem. Int. Ed*. **44,** 6996-7023 (2005).

37. Cable, R. E. & Schaak, R.E. Low-Temperature Solution Synthesis of Nanocrystalline Binary Intermetallic Compounds Using the Polyol Process. *Chem. Mater.* **17**, 6835-684 (2005).

38. Chou, N. H.& Schaak, R.E. A Library of Single-Crystal Metal-Tin Nanorods : Using Diffusion as a Tool for Controlling the Morphology of Intermetallic Nanocrystals. *Chem. Mater.* **20,** 2081-2085 (2008).

39. McBride, J., Treadway, J. Feldman, L.C. Pennycook, S.J. & Rosenthal, S.J. Structural Basis for Near Unity Quantum Yield Core/Shell Nanostructures, *Nano Lett.* **6,** 1496-1501 (2006).

40. Bond, G.C. The Electronic Structure of Platinum-Gold Alloy Particles. *Platimun Metals Rev*. **51,** 63-68 (2007).

41. Dhéron, L. *et al.* Transfer Mechanisms upon Lithium Deintercalation from LiCoO2 to CoO2 Investigated by XPS. *Chem. Mater*. **20,** 538-590 (2008).

42. Sun, H. et al. Solvothermal Synthesis of Tunable Electroactive Magnetite Nanorods by Controlling the Side Reaction. *J. Phys. Chem. C* **116,** 5476-5481 (2012).

43. Palchoudhury, S. et al. Synthesis and Growth Mechanism of Iron Oxide Nano Whiskers. *Nano Lett.* **11,** 1496-1501 (2011).

44. Suda, M. & Einaga, Y. Sequential Assembly of Phototunable Ferromagnetic Ultrathin Films with Perpendicular Magnetic Anisotropy. *Angew. Chem. Int. Ed*. **48,** 1754-1757 (2009).

45. Schlossmacher, P., Klenov, D. O.,Freitag, B. & Von Harrach, H. S. *Mater Today*, **18,** 14-20 (2010).

46. D. A. Shirley. High-Resolution X-Ray Photoemission Spectrum of the Valence Bands of Gold. *Phys. Rev. B* **5,** 4709-4714 (1972).

47. J. H. Scofield. Hartree-Slater Subshell Photoionization Cross-Sections at 1254 and 1487 eV. *J. Electron Spectrosc. Relat. Phenom*. **8,** 129-137 (1976).

.

.